photonics

MDPI

Communication

Simulated Studies of Polarization-Selectivity Multi-Band Perfect Absorber Based on Elliptical Metamaterial with Filtering and Sensing Effect

Yinghua Wang [1,*], Yubo Kong [1], Shitong Xu [1], Jie Li [2] and Guangqiang Liu [1,*]

[1] Shandong Provincial Key Laboratory of Laser Polarization and Information Technology, School of Physics and Physical Engineering, Qufu Normal University, Qufu 273165, China; kong_yb@163.com (Y.K.); xushitong@qfnu.edu.cn (S.X.)

[2] Grünberg Research Centre, Nanjing University of Posts and Telecommunications, Nanjing 210023, China; lijie@njupt.edu.cn

* Correspondence: wyh121@qfnu.edu.cn (Y.W.); gqliu@qfnu.edu.cn (G.L.)

Abstract: In this work, the Ag-SiO_2-Ag metamaterial with elliptical nano-slits was proposed to investigate the multi-band polarization-dependent perfect absorber. It was found that multi-band perfect absorptions can be induced under TE and TM-polarized illuminations. Simulation results showed that the absorption peaks for TE-polarized wave appeared at 337.6 THz and 360.0 THz with 98.5% and 97.6% absorbance, respectively. Conversely, the absorption peaks for TM-polarized wave appeared at 325.7 THz and 366.1 THz with 96.3% and 97.9% absorbance, respectively. As a result, the elliptical metamaterial presented polarization-selectivity property for perfect absorption, and so, the metamaterial can filter out different frequencies of TE- and TM-reflected waves, i.e., the elliptical metamaterial can be used as a reflecting filter. In addition, this work studied the sensing performance of the elliptical metamaterial and showed that the dual-band sensing performances were different at low and high frequencies. The sensitivities (S) to the refractive index reached up to 151.1 THz/RIU and 120.8 THz/RIU for the TE and TM-polarized waves around 337.6 THz and 325.7 THz, which provide promising potential in near-infrared photoelectric sensor and detector. However, both the absorption frequency and intensity of TM-polarized wave were insensitive to the refractive index of the medium around 366.1 THz, and so, the study provides a theoretical basis for infrared stealth of different media.

Keywords: metamaterial; perfect absorber; filtering; sensing

Citation: Wang, Y.; Kong, Y.; Xu, S.; Li, J.; Liu, G. Simulated Studies of Polarization-Selectivity Multi-Band Perfect Absorber Based on Elliptical Metamaterial with Filtering and Sensing Effect. *Photonics* **2023**, *10*, 295. https://doi.org/10.3390/photonics10030295

Received: 2 February 2023
Revised: 26 February 2023
Accepted: 7 March 2023
Published: 11 March 2023

1. Introduction

Metamaterials, composed of artificial subwavelength structures, could reshape the effective electric permittivity ε (ω) and magnetic permeability μ (ω) by freely adjusting the shape, size, and arrangement of the structures, and then, the electromagnetic waves can be flexibly controlled to achieve a novel physical effect inexistent in natural materials [1,2]. In recent years, different kinds of metamaterials configuration were proposed, including substrate-metallic materials [3], substrate-tunable dielectric materials [4–6], and metal-substrate-tunable dielectric materials [7]. In addition, various subwavelength structures, such as split-ring resonators [8], Fabry–Perot-like resonators [9], four cross resonators [10,11], and L-shaped metallic antennas [12,13], were designed. So, the exotic and unusual physical effects, such as polarization conversion, negative refraction, electromagnetically induced transparency, and perfect absorption, were realized [14–16]. As a result, there are many applications of metamaterials; for example, metamaterials were used in the antenna-senor antenna [17], beamsteering [18], transmit array [19], sensing effects in environments [20], and spatial filters [21].

As we know, the real part of the effective electric permittivity ε (ω) and magnetic permeability μ (ω) play an important role in negative refraction and many other electromagnetic effects. However, the imaginaries of μ (ω) and ε (ω) attracted much attention, attributed to the vital function of perfect absorption [2]. Perfect absorption here means a complete absorbance without transmittance and reflectance when the light incident into a material. Traditionally, the femtosecond fabrication method was used to organize absorption; however, the samples were generally large [22]. In order to obtain the subwavelength perfect absorber, the metamaterials were considered. In 2008, Landy et al. proposed a perfect metamaterial absorber for the first time in the microwave range. In the same year, Tao et al. realized the narrow-band perfect absorption at 1.12 THz with a maximum value of 98%. Recently, the narrow-band response was used to increase the Q-factor, the figure of merit (FOM), and sensitivity; as a result, the perfect absorber could be used in sensing [11,23]. Here, perfect metamaterial absorbers are weight light, size small, and controllable in absorbance and frequencies, which provide potential applications in detectors, sensors, and energy collectors [24–26]. Therefore, the studies of perfect absorbers have extended to a dual-band, multi-band, and broad-band covering microwave, THz, infrared, and visible regions. In 2010, a dual-band absorber consisting of a metallic plane, a dielectric middle layer, and two split-ring resonators was designed firstly by Tao et al. The absorption was 85% and 94% at 1.8 and 2.97 THz, respectively [27]. Then, Zhou et al. realized the dual-band perfect absorber in the microwave range with the absorption of 97% and 94% [28]. Subsequently, the dual-band infrared and visible perfect absorber based on metal-dielectric-metal (sandwich) structures were studied by Yi et al. and the absorption was increased to more than 99% [29,30]. Compared with the single narrow-band and dual-band absorption, multiple frequency resonances could develop multi-band absorption. Therefore, combining more resonators and stacking multi-layer structures was demonstrated to realize the multi-band perfect absorber [31–33]. In 2013, Lee et al. proposed a triple- and quad-band perfect absorber in the microwave region, based on the arrangement of donut-type resonators [34]. In addition, the triple-band metamaterial absorber based on three resonators was studied in THz by Li et al. [35]. To reduce the number of metallic resonators and maintain the multi-band perfect absorption effect, cross-shaped resonators were proposed [36,37]. More importantly, different kinds of metals and mediums, such as nickel, GST, Al-doped ZnO, or graphene, were considered to enhance the absorption efficiency, broaden the band of perfect absorption, and simplify the structures [38–43]. In addition, filtering and sensing are important applications of the perfect absorbers. In 2020, sensing property was studied by Chen et al., and the results showed that the sensitivities were 25.3, 41.3, and 31.9 THz/RIU for the triple-band, which were significantly less than the single narrow band perfect absorbers when the refractive index of surroundings were changed [29]. Therefore, it is necessary to enhance the sensitivity of sensing performance for multi-band perfect absorbers. In addition, polarization is an important part of electromagnetic waves, and the study of polarization increased in popularity [44,45]. In recent years, a wideband frequency-selective surface bandpass filter for TE and TM polarizations was realized based on all-metal metamaterial [46]. However, for perfect absorbers, many works paid attention to increasing the symmetry of the metamaterial to obtain the polarization-insensitive absorbers [47–49]. So, the polarization selection effect was limited and, as a result, the filtering effect for different polarizations could not be realized by the symmetry-perfect absorbers.

In this work, we present a multi-band perfect absorber with the polarization-selective character, which was composed of an Ag-dielectric (SiO_2)-Ag triple-layer film with periodic elliptical air gaps embedding in the top Ag layer. Simulation results demonstrated that quad-band perfect absorption was achieved when TE- and TM-polarized waves illuminated normally. Coincidentally, the polarization-selective character can be used as a reflecting filter. More importantly, we studied the sensing property of the multi-band perfect absorber, and the result showed that the sensitivities were 151.1 THz/RIU and 120.8 THz/RIU for TE- and TM-polarized waves, respectively. Finally, the elliptical perfect absorber had good

geometric parameters tolerance, which facilitates sample fabrication and provides more potential in the application of sensors and filters.

2. Structure Design and Method

Figure 1a presents the schematic diagram of the multi-band polarization-sensitive perfect absorber with periodic elliptical nano-slits arranged as p = 750 nm. Here, the nano-slits were induced by embedding an elliptical air gap into the top silver (Ag) thin film with the thickness t = 90 nm. The anisotropic design of nano-slits can excite different localized surface plasmon (LSP) resonant modes for TE- and TM-polarized waves illuminating along –z direction. Additionally, the bottom layer was to reflect waves by an Ag plane (t_1 = 150 nm) without nanostructures. Then, a SiO_2 (ε_{sio_2} = 2.1) spacer with d = 200 nm was set in the middle layer to connect the top and the bottom Ag layer. Figure 1b shows the perspective view of the unit cell with Ag-SiO_2-Ag configuration. The inner radius and width of the elliptical nano-slit were a = 43 nm, b = 86 nm, and w = 50 nm [Figure 1c]. The perfect absorption can be simulated by the Frequency Domain Solver based on CST Microwave Studio. In the simulation, the boundary conditions were periodic in $\pm x$ and $\pm y$ directions, while an open boundary was used in the $\pm z$ direction. Here, the minimum edge length was 2.67 nm, the maximum edge length was 158.53 nm, and the number of mesh cells was 66,322. All the designs guaranteed the accuracy of simulation results.

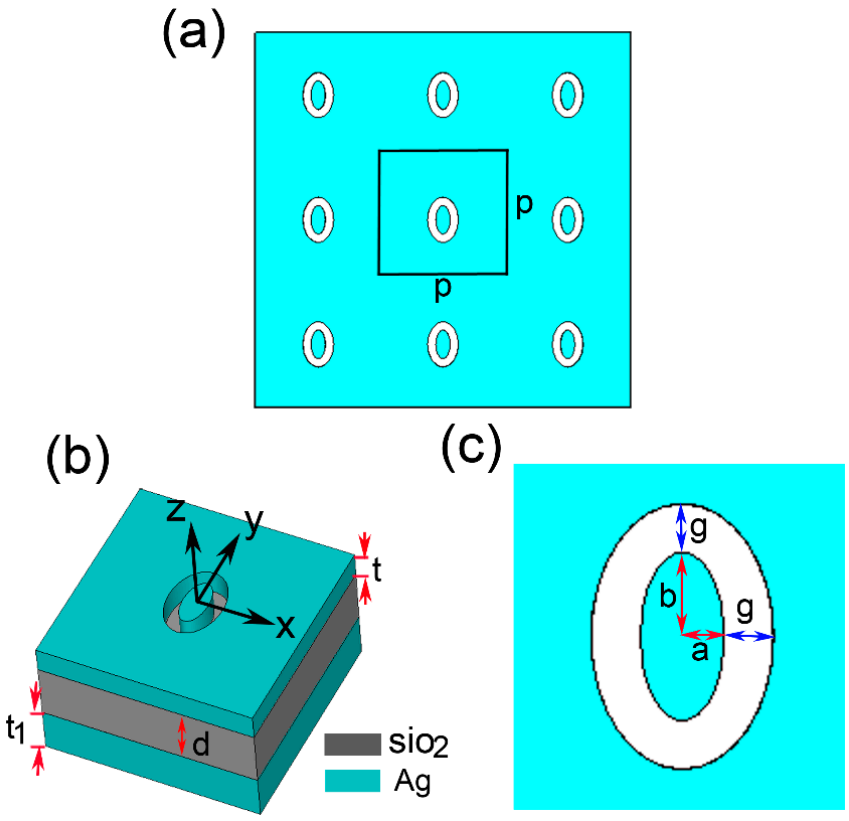

Figure 1. (**a**) Schematic diagram of periodic elliptical nano-slits. (**b**) A perspective view of the unit cell with Ag-Sio_2-Ag configuration. (**c**) A front view of a single elliptical nano-slit with a = 43 nm, b = 86 nm, g = 50 nm.

The top and bottom Ag layers were considered as Drude-type dispersion:

$$\varepsilon(\omega) = \varepsilon_\infty - \frac{\omega_p^2}{(\omega^2 + i\omega\gamma)}$$

Here, the high-frequency permittivity, plasma frequency, and collision frequency were $\varepsilon_\infty = 6.0$, $\omega_p = 1.37 \times 10^{16} s^{-1}$, and $\gamma = 7.73 \times 10^{13} s^{-1}$, respectively [3].

3. Result and Discussion

Figure 2 displays the simulated transmittance, reflectance, and absorbance spectra. From Figure 2a, we observed that two resonant dips appeared at 337.6 THz and 360.0 THz, with the reflectance (R) of about 1.5% and 2.4%, according to the TE-polarized wave. Variously, the resonances occurred at 325.7 THz and 366.1 THz with the reflectance of about 3.7% and 2.1%, according to the TM-polarized wave. Owing to the skin depth of electromagnetic waves, the transmission distances in Ag film were less than 150 nm for the high-frequency TE- and TM-polarized waves. As a result, the transmittances (T) were zero for TE- and TM-polarized waves [Figure 2a]. Figure 2b shows the absorbance (A) defined by: A = 1 − R − T [1,30]. The maximum values of absorbance achieved 98.5% and 97.6% for TE-polarized waves at 337.6 THz and 360.0 THz, respectively. In addition, the maximum values of absorbance achieved 96.3 % and 97.9% for TM-polarized waves at 325.7 THz and 366.1 THz, respectively. As a result, our proposed elliptical metamaterial acted as a perfect absorber both for TE- and TM-polarized waves. Here, the anisotropy of the elliptical nano-slits resulted in selective absorption of TE- and TM-polarized, and then the reflectances were also selective. In addition, the TE-polarized wave was mostly reflected at 325.7 and 366.1 THz, while the TM-polarized wave was mostly reflected at 337.6 and 360.0 THz. As a result, the perfect absorber can also be used as a reflecting filter.

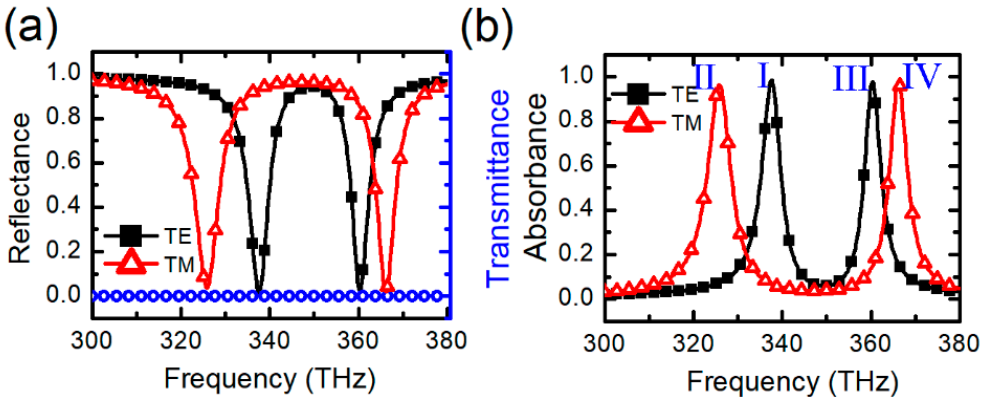

Figure 2. (**a**) Simulated reflectance and transmittance curves for TE- and TM-polarized waves illuminate on elliptical metamaterial, respectively. (**b**) The corresponding absorbance of TE- and TM-polarized waves.

To analyze the physical mechanism of the dual-band perfect absorption, we prepared electric field monitors at 337.6 THz, 360.5 THz, 326 THz, and 366 THz, respectively. Then, the three-dimensional electric field vectors could be stored. To better analyze the electric field distribution on elliptical nano-slits, we projected the electric field distribution onto the *xoy* plane [Figure 3]. Figure 3a–b show that the normalized electric field mainly distributed in the *y*-direction for TE-polarized wave. The resonant mode at f = 337.6 THz indicated that the electric field distributed at the outside edge of the elliptical air silt and the elliptical disk along the *y*-direction, resulting in the surface resonant mode I [Figure 3a]. Additionally, the electric fields were located in the elliptical air silt and elliptical disk, resulting in the localized resonant mode III along the *y*-direction at 360.5 THz [Figure 3b]. As a result, the TE-wave was trapped in the *y*-direction by the elliptic ring at 337.6 and 360.5 THz, thus realizing perfect absorption at the two different frequencies. Figure 3c–d show that the normalized electric field mainly distributed in the *x*-direction for the TM-polarized wave. Similar to the TE-polarized wave, here, the surface resonant mode II achieved at f = 326.0 THz with the electric fields distributed at the outside edge of the elliptical air silt and the elliptical disk along the *x*-direction, resulting in perfect absorption at f = 326.0 THz [Figure 3c]. However, the resonance at high frequency was different from the TE-polarized

mode. Figure 3d presents a localized resonant mode IV with electric-field distribution in the elliptical air slit and at the outside edge of the elliptical ring along the *x*-direction, generating the perfect absorption at f = 366.0 THz. In our design, the elliptical nano-slit was anisotropic in *x*- and *y*- directions, which was beneficial for developing different resonant modes at different frequencies with TE- and TM-polarized wave illumination. So, perfect absorption and filtering were much more evident than in previous works [30,36,37].

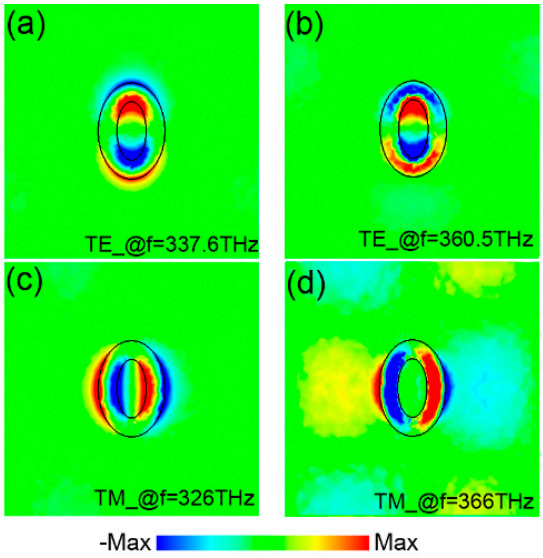

Figure 3. Electric-field distributions at resonant frequencies in the *xoz* plane (*z* =45 nm). TE-polarized wave at (**a**) f = 337.6 THz and (**b**) f = 360.5 THz. TM-polarized wave at (**c**) f = 362.0 THz and (**d**) f = 366.0 THz.

To explore the perfect absorption further, we prepared frequency monitors of power loss density (PLD) for normal incident TE- and TM-polarized waves at f = 337.6/360.5 THz and f = 326.0/366.0 THz, which could take into account any kind of dispersive materials, and then, the sum of the electric and magnetic power dissipated inside these materials could be recorded. Evidently, the power of incident light was confined more in the Ag-SiO_2-Ag metamaterial, when the PLD was high. As a result, we obtained a higher absorption efficiency. After a comparison of the four PLD results in Figure 4a–d, we observed that the elliptical slit lead to the maximal PLD at the low resonant frequencies for TE- and TM-polarized waves; as a result, the PLD mainly distributed in the top silver surface in the elliptical slit [Figure 4a,c]. Figure 4b–d show that the interaction between the top and bottom layers was strong at high frequencies, so the PLD distributed not only in the elliptical slit, but also on the surface of the top and bottom layers. Depending on the discussion above, the surface resonant modes I and II resulted in the PLD at low frequencies, and then, the perfect absorption at 337.6 and 326.0 THz originated. However, the localized resonant modes III and IV localized in elliptical slits and resonant couplings between the top and bottom Ag layer lead to the PLD at high frequencies originating with perfect absorption at 360.5 and 366.0 THz.

Then, we investigated how the different geometric parameters including the short radius (a), period (p), top Ag layer thickness (t), and elliptical slit gap (g) affected our dual-band polarization-sensitive perfect absorption; the simulated results of TE- and TM-polarized wave are shown in Figures 5 and 6, respectively. Here, we changed only one geometric parameter and kept others invariable. Figure 5a shows the absorbance spectra with different short radii (a) for TE-polarized waves. The two resonance absorbance peaks were sensitive to the geometric parameters a. The maximum absorbance values appeared at a = 43 nm, while the two resonance absorbance peaks decreased to zero with a = 0 nm, i.e., an elliptical nanohole could not induce any absorbance for TE-polarized wave. By contrast, Figure 6a shows the absorbance spectra with different short radii (a) for TM-polarized

waves. Additionally, the two resonance absorbance peaks increased to the maximum values of 98.60% and 99.96% at 335.1 THz and 372.8 THz with a = 0 nm, i.e., the nanohole was much superior in perfect absorption for TM-polarized waves. At the same time, the elliptical nanohole is much more convenient for sample fabrication in future experiments. So, the elliptical design provides more application possibilities than the proposed nanoring grooves design [2,30].

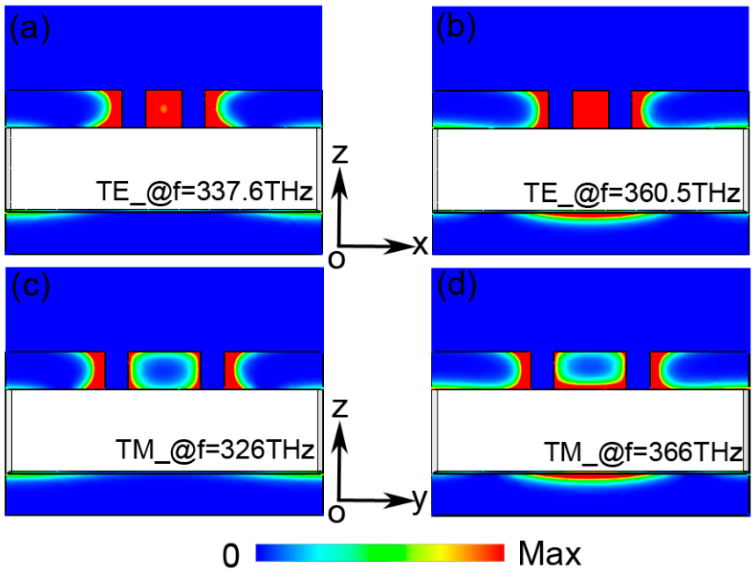

Figure 4. Power loss density at resonant frequencies (**a**) f = 337.6 THz and (**b**) f = 360.5 THz in the *xoz* plane for TE-polarized wave. Power loss density at resonant frequencies (**c**) f = 326 THz and (**d**) f = 366 THz in *yoz* plane for TM-polarized wave.

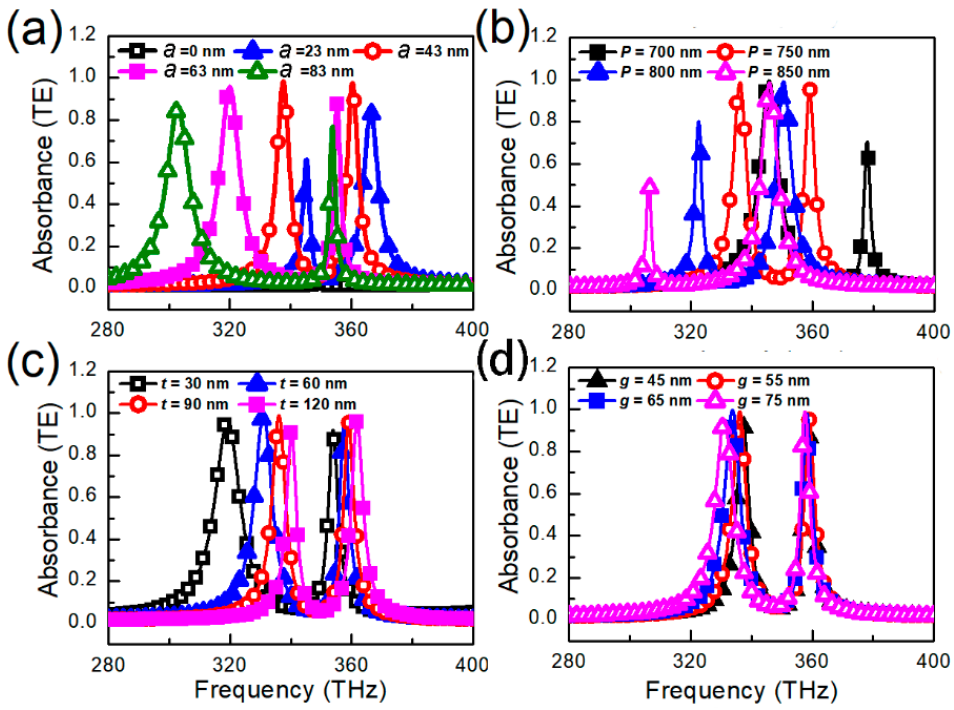

Figure 5. Absorbance spectra depending on the radius a (**a**), period p (**b**) thickness t (**c**), and elliptical silt gap g (**d**) of perfect absorber for TE-polarized wave.

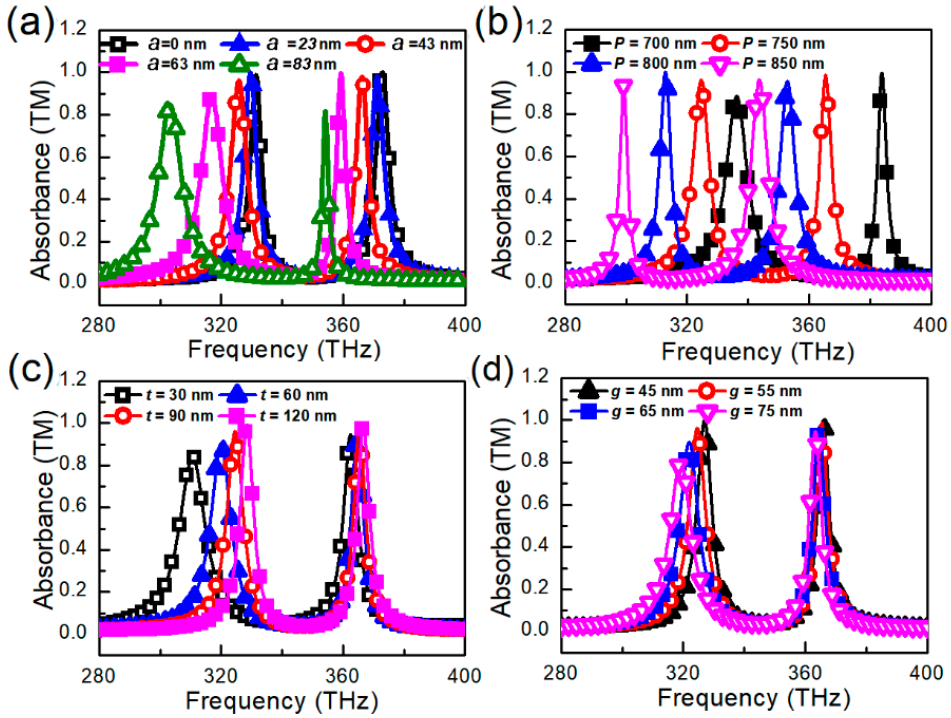

Figure 6. Absorbance spectra based on the radius *a* (**a**), period *p* (**b**) thickness *t* (**c**), and elliptical slit gap *g* (**d**) of perfect absorber for TM-polarized wave.

Figure 5b shows the relationship between the absorbance spectra and the period *p* of the elliptical slit for the TE-polarized wave. Firstly, a red-shift of the absorbance spectra with changing *p* from 700 nm to 850 nm by the step of 50 nm was observed. Secondly, the resonance absorbance peaks I and III presented the opposite relationship with the *p* changing, i.e., with the increase in the period *p*, resonance mode I decreased, but resonance mode III increased; as a result, the two resonance modes played maximum values at *p* = 750 nm. For the TM-polarized wave, the elliptical metamaterial played robust perfect absorption with changing *p*. Here, the two values of perfect absorption were nearly maintained at more than 90% and the absorbance spectra showed a red-shift with changing *p* from 700 to 850 nm [Figure 6b].

As presented in Figure 5c, the intensity of the absorption peak remained roughly the same both for TE- and TM-polarized waves by changing the thickness *t* of the top Ag layer from 30 nm to 120 nm. However, the absorbance spectra shifted to the high frequencies, i.e., the frequencies of absorbance peaks I and III appeared blue-shift. Fortunately, the TM-polarized wave provided the same property as the TE-polarized wave when the thickness *t* changed [Figure 6c]. By contrast, the absorption peaks shifted from 337 THz to 301 THz for TE-polarized waves, when the *a* increased from 43 nm to 83nm (see Figures 5d and 6d). Meanwhile, the absorption peaks shifted from 337 THz to 301 THz, when the *a* increased from 0 nm to 83 nm. To conclude, we can broaden the absorption effect by stacking elliptic nanoslit metal layers with different a, i.e., the bandwidth covered from 301 THz to 337 THz. Moreover, it was also found that, by changing the bottom Ag layer thickness t_1, the values and frequencies of perfect absorption roughly remained for TE- and TM-polarized waves (not shown in the figures). Finally, it is worth exploring the influences of the elliptical slit gap *g* on perfect absorption. As shown in Figure 5d, as the gap gradually increased from 45 nm to 75 nm by the step of 10 nm, the values and frequencies of perfect absorption remained insensitive to the gap *g* for the TE-polarized wave. For the TM-polarized wave, only the absorbance peak III showed a slight decrease, with *g* increasing from 45 nm to 75, while the values of perfect absorption remained at 80%, with *g* = 75 nm [Figure 6d]. Compared with the work reported earlier, the slit gap of our work was bigger, and the

perfect absorption was robust, and so, the fault tolerance could potentially be bigger in future sample fabrications [2].

To explore the sensing performance of this elliptical perfect absorber, we studied the absorbance spectra by changing the refractive index of the surroundings; the results are presented in Figure 7. Figure 7a shows the absorbance spectra of TE-polarized wave, the values of absorbance peaks I could have remained over 98.5% when the refractive index n of surrounding changed from 1.0 to 1.4, while the frequencies of absorbance peaks I met with obvious red-shift. Additionally, the absorbance peaks III experienced a dramatic decrease with slight red shifting, when n changed from 1.0 to 1.4. For the absorbance peaks I, the electric field distributed on the surface of the top Ag layer; as a result, the refractive index n only influenced the resonance frequencies. On the contrary, the resonant mode II was localized in the elliptical slit and coupled to the bottom Ag layer, and so, the values of absorbance peaks were evidently influenced. Compare with the TE-polarized wave, the absorbance peaks II for the TM-polarized wave experienced obvious red-shift with n changing; meanwhile, the absorbance peaks IV provided slight value change and red-shift when n changed from 1.0 to 1.4. As we know, the sensing capability of the elliptical metamaterial can be defined by sensitivity (S) [11,37]: $S = \Delta f / \Delta n$, where Δf and Δn are the change of the resonance frequency and refractive index value, respectively. Compared with the reported absorber in the near-infrared region [9,10,37], our proposed elliptical metamaterial provided excellent sensing performance both for TE- and TM-polarized waves with the S of resonant modes I and II reaching up to 151.1 THz/RIU (483.3 nm/RIU) and 120.8 THz/RIU (400.2 nm/RIU), respectively [Figure 6c]. So, the elliptical metamaterial can be used in sensor fields.

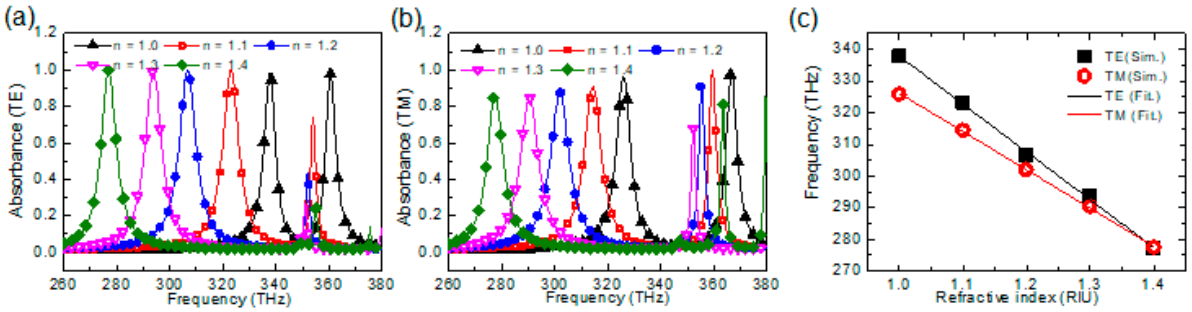

Figure 7. Absorbance spectra depending on different refractive indices (n) of surroundings for (**a**) TE-polarized wave and (**b**) TM-polarized wave. (**c**) Simulated (symbols) and linear fit (line) resonance frequencies as a function of n.

4. Conclusions

In conclusion, we proposed a simple multi-band polarization-sensitive perfect absorber based on a periodic elliptical slit with good slit gap tolerance. The simulated results indicated that four absorbance peaks (f_1 = 337.7 THz, f_2 = 360.6 THz, f_3 = 325.7 THz, and f_4 = 366.1 THz) with the values of 98.5%, 97.6%, 96.3%, 97.9% were realized. Meanwhile, every absorbance peak could be increased to greater than 99% by optimizing different geometric parameters. In addition, the perfect absorption was sensitive to polarization, i.e., the perfect absorption at f_1 = 337.7 THz/f_2 = 360.6 THz and f_3 = 325.7 THz/f_4 = 366.1 THz were achieved by TE- and TM-polarized waves, respectively.

Author Contributions: Y.W., conceptualization, data curation, writing—original draft; Y.K., software; S.X., investigation, writing—review and editing; J.L., formal analysis; G.L., supervision, visualization, writing—review and editing. All authors have read and agreed to the published version of the manuscript.

Funding: National Natural Science Foundation of China (NSFC) (Nos. 11904200, 62005143, 51871208), Natural Science Foundation of Jiangsu Province (BK20190726).

Institutional Review Board Statement: Not applicable.

Informed Consent Statement: Not applicable.

Data Availability Statement: No data were generated or analyzed in the presented research.

Conflicts of Interest: The authors declare no conflict of interest.

References

1. Landy, N.I.; Sajuyigbe, S.; Mock, J.J.; Smith, D.R.; Padilla, W.J. Perfect metamaterial absorber. *Phys. Rev. Lett.* **2008**, *100*, 207402. [CrossRef]
2. Li, J.; Wang, Y.-H.; Jin, R.-C.; Li, J.-Q.; Dong, Z.-G. Toroidal-dipole induced plasmonic perfect absorber. *J. Phys. D Appl. Phys.* **2017**, *50*, 485301. [CrossRef]
3. Wang, Y.-H.; Jin, R.-C.; Li, J.-Q.; Zhong, F.; Liu, H.; Kim, I.; Jo, Y.; Rho, J.; Dong, Z.-G. Photonic spin Hall effect by the spin-orbit interaction in a metasurface with elliptical nanostructures. *Appl. Phys. Lett.* **2017**, *110*, 101908. [CrossRef]
4. Qi, Y.; Zhang, Y.; Liu, C.; Zhang, T.; Zhang, B.; Wang, L.; Deng, X.; Bai, Y.; Wang, X. A tunable terahertz metamaterial absorber composed of elliptical ring graphene arrays with refractive index sensing application. *Results Phys.* **2020**, *16*, 103012. [CrossRef]
5. Norouzi, M.; Jarchi, S.; Ghaffari-Miab, M.; Esfandiari, M.; Lalbakhsh, A.; Koziel, S.; Reisenfeld, S.; Moloudian, G. 3D metamaterial ultra-wideband absorber for curved surface. *Sci. Rep.* **2023**, *13*, 1043. [CrossRef] [PubMed]
6. Esfandiari, M.; Lalbakhsh, A.; Shehni, P.N.; Jarchi, S.; Ghaffari-Miab, M.; Mahtaj, H.N.; Reisenfeld, S.; Alibakhshikenari, M.; Koziel, S.; Szczepanski, S. Recent and emerging applications of Graphene-based metamaterials in electromagnetics. *Mater. Des.* **2022**, *221*, 110920. [CrossRef]
7. Feng, Q.-Y.; Yan, D.-X.; Li, X.-J.; Li, J.-N. Realization of absorption, filtering, and sensing in a single metamaterial structure combined with functional materials. *Appl. Opt.* **2022**, *61*, 4336–4343. [CrossRef]
8. Gu, S.; Barrett, J.; Hand, T.H.; Popa, B.; Cummer, S.A. A broadband low-reflection metamaterial absorber. *J. Appl. Phys.* **2010**, *108*, 064913. [CrossRef]
9. Hu, S.; Yang, S.; Liu, Z.; Quan, B.; Li, J.; Gu, C. Broadband and polarization-insensitive absorption based on a set of multisized Fabry–Perot-like resonators. *J. Phys. Chem. C* **2019**, *123*, 13856–13862. [CrossRef]
10. Ma, W.; Wen, Y.; Yu, X. Broadband metamaterial absorber at mid-infrared using multiplexed cross resonators. *Opt. Express* **2013**, *21*, 30724–30730. [CrossRef]
11. Hu, D.; Meng, T.; Wang, H.; Ma, Y.; Zhu, Q. Ultra-narrow-band terahertz perfect metamaterial absorber for refractive index sensing application. *Results Phys.* **2020**, *19*, 103567. [CrossRef]
12. Zhang, J.; Zhang, K.; Cao, A.; Liu, Y.; Kong, W. Bi-functional switchable broadband terahertz polarization converter based on a hybrid graphene-metal metasurface. *Opt. Express* **2020**, *28*, 26102–26110. [CrossRef] [PubMed]
13. Chen, Z.; Chen, H.; Jile, H.; Xu, D.; Yi, Z.; Lei, Y.; Chen, X.; Zhou, Z.; Cai, S.; Li, G. Multi-band multi-tunable perfect plasmon absorber based on L-shaped and double-elliptical graphene stacks. *Diam. Relat. Mater.* **2021**, *115*, 108374. [CrossRef]
14. Wang, Y.-H.; Kong, Y.-B.; Li, J.; Xu, S.-T.; Zhang, X.; Dong, Z.-G. Dual-band polarization conversions and optical diode based on bilayer T-shaped metamaterial. *Results Phys.* **2022**, *42*, 105981. [CrossRef]
15. Song, Z.; Chen, A.; Zhang, J.; Wang, J. Integrated metamaterial with functionalities of absorption and electromagnetically induced transparency. *Opt. Express* **2019**, *27*, 25196–25204. [CrossRef] [PubMed]
16. Zhu, H.; Zhang, Y.; Ye, L.; Li, Y.; Xu, Y.; Xu, R. Switchable and tunable terahertz metamaterial absorber with broadband and multi-band absorption. *Opt. Express* **2020**, *28*, 38626–38637. [CrossRef]
17. Esfandiyari, M.; Lalbakhsh, A.; Jarchi, S.; Ghaffari-Miab, M.; Mahtaj, H.N.; Simorangkir, R.B. Tunable terahertz filter/antenna-sensor using graphene-based metamaterials. *Mater. Des.* **2022**, *220*, 110855. [CrossRef]
18. Das, P.; Mndal, K.; Lalbakhsh, A. Beam-steering of microstrip antenna using single-layer FSS based phase-shifting surface. *Int. J. RF Microw. Computer-Aided Eng.* **2022**, *32*, e23033. [CrossRef]
19. Lalbakhsh, A.; Afzal, M.U.; Hayat, T.; Esselle, K.P.; Mandal, K. All-metal wideband metasurface for near-field transformation of medium-to-high gain electromagnetic sources. *Sci. Rep.* **2021**, *11*, 9421. [CrossRef]
20. Lalbakhsh, A.; Simorangkir, R.B.; Bayat-Makou, N.; Kishk, A.A.; Esselle, K.P. Advancements and artificial intelligence approaches in antennas for environmental sensing. *Artif. Intell. Data Sci. Environ. Sens.* **2022**, 19–38.
21. Paul, G.S.; Mandal, K.; Lalbakhsh, A. Single-layer ultra-wide stop-band frequency selective surface using interconnected square rings. *AEU Int. J. Electron. Commun.* **2021**, *132*, 153630. [CrossRef]
22. Kudryashov, S.; Nastulyavichus, A.; Krasin, G.; Khamidullin, K.; Boldyrev, K.; Kirilenko, D.; Yachmenev, A.; Ponomarev, D.; Komandin, G.; Lebedev, S.; et al. CMOS-compatible direct laser writing of sulfur-ultrahyperdoped silicon: Breakthrough pre-requisite for UV-THz optoelectronic nano/microintegration. *Opt. Laser Technol.* **2023**, *158*, 108873. [CrossRef]
23. Pan, M.; Su, Z.; Yu, Z.; Wu, P.; Jile, H.; Yi, Z.; Chen, Z. A narrowband perfect absorber with high Q-factor and its application in sensing in the visible region. *Results Phys.* **2020**, *19*, 103415. [CrossRef]
24. Wang, Y.; Sun, T.; Paudel, T.; Zhang, Y.; Ren, Z.; Kempa, K. Metamaterial-plasmonic absorber structure for high efficiency amorphous silicon solar cells. *Nano Lett.* **2012**, *12*, 440–445. [CrossRef] [PubMed]
25. Rephaeli, E.; Fan, S. Absorber and emitter for solar thermo-photovoltaic systems to achieve efficiency exceeding the Shockley-Queisser limit. *Opt. Express* **2009**, *17*, 15145–15159. [CrossRef] [PubMed]

26. Liu, N.; Mesch, M.; Weiss, T.; Hentschel, M.; Giessen, H. Infrared perfect absorber and its application as plasmonic sensor. *Nano Lett.* **2010**, *10*, 2342–2348. [CrossRef]
27. Tao, H.; Bingham, C.M.; Pilon, D.; Fan, K.; Strikwerda, A.C.; Shrekenhamer, D.; Padilla, W.J.; Zhang, X.; Averitt, R.D. A dual band terahertz metamaterial absorber. *J. Phys. D Appl. Phys.* **2010**, *43*, 225102. [CrossRef]
28. Liu, X.; Lan, C.; Bi, K.; Li, B.; Zhao, Q.; Zhou, J. Dual band metamaterial perfect absorber based on Mie resonances. *Appl. Phys. Lett.* **2016**, *109*, 062902. [CrossRef]
29. Zhang, Y.; Yi, Z.; Wang, X.; Chu, P.; Yao, W.; Zhou, Z.; Cheng, S.; Liu, Z.; Wu, P.; Pan, M.; et al. Dual band visible metamaterial absorbers based on four identical ring patches. *Phys. E* **2021**, *127*, 114526. [CrossRef]
30. Liang, C.; Yi, Z.; Chen, X.; Tang, Y.; Yi, Y.; Zhou, Z.; Wu, X.; Huang, Z.; Yi, Y.; Zhang, G. Dual-band infrared perfect absorber based on a Ag-dielectric-Ag multilayer films with nanoring grooves arrays. *Plasmonics* **2020**, *15*, 93–100. [CrossRef]
31. Wang, Y.; Chen, Z.; Xu, D.; Yi, Z.; Chen, X.; Chen, J.; Tang, Y.; Wu, P.; Li, G.; Yi, Y. Triple-band perfect metamaterial absorber with good operating angle polarization tolerance based on split ring arrays. *Results Phys.* **2020**, *16*, 102951. [CrossRef]
32. Zhang, K.; Xia, F.; Li, S.; Liu, Y.; Kong, W. Actively tunable multi-band terahertz perfect absorber due to the hybrid strong coupling in the multilayer structure. *Opt. Express* **2021**, *29*, 28619–28630. [CrossRef] [PubMed]
33. Meng, T.; Hu, D.; Zhu, Q. Design of a five-band terahertz perfect metamaterial absorber using two resonators. *Opt. Commun.* **2018**, *415*, 151–155. [CrossRef]
34. Park, J.W.; Van Tuong, P.; Rhee, J.Y.; Kim, K.W.; Jang, W.H.; Choi, E.H.; Chen, L.Y.; Lee, Y. Multi-band metamaterial absorber based on the arrangement of donut-type resonators. *Opt. Express* **2013**, *21*, 9691–9702. [CrossRef]
35. Wang, R.; Li, L.; Liu, J.; Yan, F.; Tian, F.; Tian, H.; Zhang, J.; Sun, W. Triple-band tunable perfect terahertz metamaterial absorber with liquid crystal. *Opt. Express* **2017**, *25*, 32280–32289. [CrossRef]
36. Wang, B.-X.; He, Y.; Lou, P.; Zhu, H. Multi-band terahertz superabsorbers based on perforated square-patch metamaterials. *Nanoscale Adv.* **2021**, *3*, 455–462. [CrossRef] [PubMed]
37. Cheng, Y.; Chen, F.; Luo, H. Triple-band perfect light absorber based on hybrid metasurface for sensing application. *Nanoscale Res. Lett.* **2020**, *15*, 103. [CrossRef]
38. Naveed, M.A.; Bilal, R.M.H.; Baqir, M.A.; Bashir, M.M.; Ali, M.M.; Rahim, A.A. Ultrawideband fractal metamaterial absorber made of nickel operating in the UV to IR spectrum. *Opt. Express* **2021**, *29*, 42911–42923. [CrossRef]
39. Sun, K.; Riedel, C.A.; Wang, Y.; Urbani, A.; Simeoni, M.; Mengali, S.; Zalkovskij, M.; Bilenberg, B.; de Groot, C.H.; Muskens, O.L. Metasurface optical solar reflectors using AZO transparent conducting oxides for radiative cooling of spacecraft. *ACS Photonics* **2018**, *5*, 495–501. [CrossRef]
40. Rana, A.S.; Mehmood, M.Q.; Jeong, H.; Kim, I.; Rho, J. Tungsten-based ultrathin absorber for visible regime. *Sci. Rep.* **2018**, *8*, 2443. [CrossRef]
41. Shafique, A.; Naveed, M.A.; Ijaz, S.; Zubair, M.; Mehmood, M.Q.; Massoud, Y. Highly efficient Vanadium Nitride based metasurface absorber/emitter for solar-thermophotovoltaic system. *Mater. Today Commun.* **2023**, *34*, 105416. [CrossRef]
42. Li, C.; Pan, R.; Geng, G.; Zheng, R.; Gu, C.; Guo, H.; Li, J. Strong and Omnidirectional Light Absorption from Ultraviolet to Near-Infrared Using GST Metasurface. *Laser Photonics Rev.* **2023**, *17*, 2200364. [CrossRef]
43. Huo, D.; Zhang, J.; Wang, Y.; Wang, C.; Su, H.; Zhao, H. Broadband perfect absorber based on TiN-nanocone metasurface. *Nanomaterials* **2018**, *8*, 485. [CrossRef] [PubMed]
44. Kesaev, V.; Nastulyavichus, A.; Kudryashov, S.; Kovalev, M.; Stsepuro, N.; Krasin, G. Nanopatterned silicon exhibiting partial polarization and chirality. *Opt. Mater. Express* **2021**, *11*, 1971–1977. [CrossRef]
45. Atkinson, G.A.; Ernst, J.D. High-sensitivity analysis of polarization by surface reflection. *Mach. Vis. Appl.* **2018**, *29*, 1171–1189. [CrossRef]
46. Lalbakhsh, A.; Afzal, M.U.; Esselle, K.P.; Smith, S.L. All-metal wideband frequency-selective surface bandpass filter for TE and TM polarizations. *IEEE Trans. Antennas Propag.* **2022**, *70*, 2790–2800. [CrossRef]
47. Li, L.; Xi, R.; Liu, H.; Lv, Z. Broadband polarization-independent and low-profile optically transparent metamaterial absorber. *Appl. Phys. Express* **2018**, *11*, 052001. [CrossRef]
48. Zhou, W.; Li, K.; Song, C.; Hao, P.; Chi, M.; Yu, M.; Wu, Y. Polarization-independent and omnidirectional nearly perfect absorber with ultra-thin 2D subwavelength metal grating in the visible region. *Opt. Express* **2015**, *23*, 413–418. [CrossRef]
49. Jing, H.; Duan, J.; Wei, Y.; Hao, J.; Qu, Z.; Wang, J.; Zhang, B. An ultra-broadband flexible polarization-insensitive microwave metamaterial absorber. *Mater. Res. Express* **2022**, *9*, 025802. [CrossRef]